



HAL
open science

Self-Organizing Artificial Intelligence Captures Landscape Changes Correlated with Human Impact Data

John Mwangi Wandeto, Birgitta Dresp

► **To cite this version:**

John Mwangi Wandeto, Birgitta Dresp. Self-Organizing Artificial Intelligence Captures Landscape Changes Correlated with Human Impact Data. 2023. hal-04345752

HAL Id: hal-04345752

<https://hal.science/hal-04345752>

Preprint submitted on 14 Dec 2023

HAL is a multi-disciplinary open access archive for the deposit and dissemination of scientific research documents, whether they are published or not. The documents may come from teaching and research institutions in France or abroad, or from public or private research centers.

L'archive ouverte pluridisciplinaire **HAL**, est destinée au dépôt et à la diffusion de documents scientifiques de niveau recherche, publiés ou non, émanant des établissements d'enseignement et de recherche français ou étrangers, des laboratoires publics ou privés.



Distributed under a Creative Commons Attribution 4.0 International License

1 *Preprint*

2 **Self-Organizing Artificial Intelligence Captures** 3 **Landscape Changes Correlated with Human Impact** 4 **Data**

5 **John M. Wandeto¹, Birgitta Dresp-Langley^{2*}**

6 ¹ Department of Information Technology, Dedan Kimathi University of Technology, Nyeri, Kenya

7 ² Centre National de la Recherche Scientifique UMR 7357 ICube Lab, Strasbourg University, France;

8 birgitta.dresp@unistra.fr

9 * Correspondence: birgitta.dresp@cnrs.fr; Tel.: +33-388119117

10 **Abstract:** Self-organization is the core principle of all learning in Adaptive Resonance Theory
11 (ART), which has been highly successful in accounting for biological visual learning, or
12 biologically plausible computational modelling of visual processing. Such processing includes the
13 analysis of visual data we may not be able to see consciously, such as changes in fine visual detail
14 in images relating to alterations in natural or urban landscapes, for example. In the course of time,
15 such imaging data may reveal structural changes that are the consequence of measurable human
16 impact or climate change. Capturing such change in time series of satellite images before the
17 human eye can see them makes them available at early stages to citizens, professionals, and
18 policymakers, promotes change awareness, and facilitates early decision making for action. Here,
19 we use unsupervised Artificial Intelligence (AI) that exploits principles of self-organized biological
20 visual learning for the analysis of time series of satellite images. The Quantization Error (QE) in
21 the output of a Self-Organizing Map prototype is exploited as a computational metric of
22 variability and change. Given the proven sensitivity of this neural network metric to the intensity
23 and polarity of image pixel contrast, and its proven selectivity to pixel colour, it is shown to
24 capture critical changes in urban landscapes. This is achieved here in the example of satellite
25 images from two regions of geographic interest in Las Vegas County, Nevada, USA across the
26 years 1984-2008. The SOM-QE analysis is combined with the statistical analysis of demographic
27 data revealing human impacts correlated with the structural changes in the specific regions of
28 interest. By correlating the impact of human activities with the structural evolution of urban
29 environments we further expand SOM-QE analysis, as a parsimonious and reliable AI approach,
30 to the rapid detection of human footprint-related environmental change.

31 **Keywords:** SatelliteImages, Landscapes, Urban Environment, Las Vegas, Self Organizing Map
32 (SOM), Quantization Error, Demographic Data, Human Impact
33

34 **1. Introduction**

35 Grossberg's Adaptive Resonance Theory proposes neural network models that enable stable
36 brain learning in non-stationary and unexpected worlds [1]. These models rely on self-organized
37 learning akin to biological synaptic learning [2, 3, 4]. In biological neural networks, such learning is
38 by nature unsupervised and may be accounted for in terms of competitive *winner-takes-all* matching
39 principles [5]. The Self-Organizing Map (SOM) is, by comparison with the ART models, a
40 parsimonious, one may call it minimalist, artificial neural network architecture [6, 7] with input-
41 driven self-organization using *winner-takes-all* learning in sensory model neurons that become
42 locally and globally ordered during learning. In our previous studies, we exploited the functional
43 properties of sensitivity to spatial extent, intensity, and colour of local pixel contrasts of the

44 Quantization Error (QE) in the output of a SOM for automatic data classification as a function of
45 finest, mostly invisible, yet, clinically or functionally relevant, local variations in visual or other data
46 time series. This work, extensively and well documented in our prior publications [8-19], has
47 permitted establishing SOM-QE [8] as a reliable computational model of statistical variability in
48 sensed data, directly relating to critical local changes in images of one and the same landscape [15],
49 of organs [19], cells [10, 13, 16], and other simulated visual objects at different moments in time [11,
50 14, 17, 18], and in temporal series of sensor responses from surgical data simulating robotic control
51 by grip forces distributed in the human hands of experts and novices [9, 12].

52 Any technique for the determination of the finest changes of visual or other sensed data across
53 time, even when combined with an advanced imaging model, sooner or later requires human
54 classification for an interpretation. This may involve guesswork when the spatiotemporal
55 uncertainty [20-22] in the data or visual image contents is high. It then becomes difficult to rule out
56 subjectivity of the analyst, even when the latter is a skilled expert. To ensure quality decision
57 making, affordable precision software for automatic data classification should combine high
58 accuracy with further advantages relative to speed, objectivity, and reproducibility of the
59 classification. All these have been proven ensured by SOM-QE within the scope of its application
60 [8]. In this work here, we show simulations exploiting SOM-QE analysis [8] to demonstrate its
61 statistically significant sensitivity to the spatial extent of local pixel contrast translating significant
62 landscape changes correlated with significant increase in human impact, and its ecological footprint
63 as a consequence [23], in response to these changes. NASA Landsat images of Las Vegas City
64 Centre and the residential North of Las Vegas from a time period between 1984 and 2008 were
65 submitted to SOM-QE analysis for this study. In the 1980ies Las Vegas City, located in the middle of
66 the Nevada Desert, featured mainly 'The Strip', with a number of smaller casinos and motels.
67 Subsequently, in a large restructuration project between 1990 and 2007 a large number of the old
68 casinos and motels were demolished. The ensuing reconstruction of Las Vegas City Centre and the
69 subsequent opening of a large number of mega-resorts with casino spaces, tropical landscapes with
70 waterfalls or simulations of urban environments such as Venice, restaurants with world-class chefs,
71 and shows performed by international megastars like Celine Dion transformed Las Vegas City
72 Centre and The Strip entirely. By offering multiple kinds of entertainment, dining gambling, and
73 lodging, attracting millions of visitors from all over the world, Las Vegas City Centre has become
74 one of the largest entertainment poles in the world [24]. Most elements of the project opened in late
75 2009. This was accompanied by the rapid spread of greater Las Vegas, including the residential
76 North, into the adjacent desert. The population count grew from thousands in 1984 to millions in
77 2009.

78 2. Materials and Methods

79 25 satellite images of the geographic regions of interest (ROI), Las Vegas City Center and
80 Residential North were pre-processed and then submitted to SOM-QE analysis. The original pre-
81 processed input images can be accessed from the Supplementary Materials.

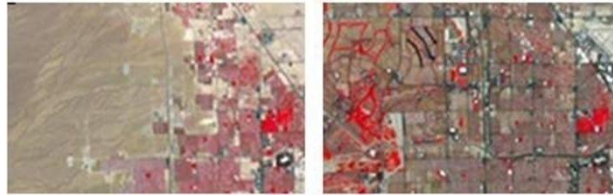
82 2.1. Image input

83 The original images were extracted from time-lapse animations of Las Vegas County, Nevada,
84 for a reference time period from 1984 to 2008, as captured by NASA Landsat sensors [25]. VLC [26],
85 an open source media player, was used to generate static images from the time-lapse animations
86 provided. The images are colour-coded for optimal visualization [27], displaying arid desert regions
87 in brownish-gray, building structures in dark-gray and healthy vegetation and green spaces in red
88 pixels. Water is represented by black pixels. Sample copies of two of the pre-processed 25 images
89 for each ROI, Las Vegas City centre (Fig.1) and residential North (Fig. 2) from the years 1984 and
90 2008 are shown here below.

91



92
93
94 **Figure 1.** Representation of two of the 25 satellite image extracts of Las Vegas city centre in 1984 (left) and 2008
95 (right), after preprocessing.
96



97
98
99
100 **Figure 2.** Representation of two of the 25 satellite image extracts of Las Vegas residential North in 1984 (left)
101 and 2008 (right), after preprocessing.
102

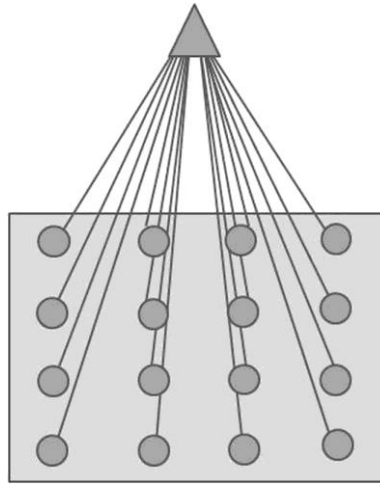
103 Before running the SOM-QE analysis on the image time series for the two geographic ROI, the
104 images were pre-processed to ensure they are all identically scaled and aligned within a given
105 series. This was achieved by applying the method of co-registration using *StackReg* [28], which is a
106 plug-in for *ImageJ*, an open source image processing program designed for scientific
107 multidimensional image processing. The last image of the time series was used to anchor the
108 registration. Control for variations in contrast strength between images of a given series was
109 performed after registration. This was achieved by increasing the image contrast and by removing
110 any local variations at different times of image acquisition [29-30]. For each extracted image,
111 contrast intensity (I) normalization was ensured using
112

$$I_{final} = (I - I_{min} / I_{max} - I_{min}) \times 255 \quad (1)$$

113
114
115 The registered and normalized image taken in 2008 from each ROI was used to train the SOM. Since
116 the original images used colour to emphasize different areas on the maps, pixel-based RGB values
117 are used as input features to the SOM. This ensures a pixel-by-pixel capture of detail and avoids
118 errors due to inaccurate feature calculation, which often occurs with complex images [30].

119 2.2. SOM-QE analysis

120 The Self-Organizing Map (the prototype for this study here is graphically represented in Fig. 3,
121 for illustration) may be described formally as a nonlinear, ordered, smooth mapping of high-
122 dimensional input data onto the elements of a regular, low-dimensional array [6, 7, 8]. It is assumed
123 that the set of input variables can be defined as a real vector x , of n -dimensionality. A parametric
124 real vector m_i of n -dimension is associated with each element in the SOM. Vector m_i is a model and
125 the SOM is therefore an array of models. Assuming a general distance measure between x and m_i
126 denoted by $d(x, m_i)$, the map of an input vector x on the SOM array is defined as the array element
127 m_c that matches best (smallest $d(x, m_i)$) with x . During the learning process, the input vector x
128 is compared with all the m_i in order to identify m_c . The Euclidean distances $\|x - m_i\|$ define m_c . Models
129 topographically close in the map up to a certain geometric distance indicated by h_{ci} will activate
130 each other to learn something from their common input x .
131



132
133

134 **Figure 3.** Graphic representation of the 4x4 SOM prototype with 16 models, indicated by the filled circles in the
135 grey box. Each of these models is compared to the SOM input in an unsupervised winner-take-all learning
136 process. The input vector corresponds to the RGB image pixel space.

137 This results in a local relaxation or smoothing effect on the models in this neighborhood, which in
138 continuous learning leads to global ordering. Self-organized learning in a SOM is represented by
139 the equation

$$140 \quad \mathbf{m}(t + 1) = \mathbf{m}_i(t) + \alpha(t)h_{ci}(t)[\mathbf{x}(t) - \mathbf{m}_i(t)] \quad (2)$$

141 where $t = 1, 2, 3, \dots$ is an integer, the discrete-time coordinate, $h_{ci}(t)$ is the neighborhood function, a
142 smoothing kernel defined over the map points which converges towards zero with time, $\alpha(t)$ is the
143 learning rate, which also converges towards zero with time and affects the amount of learning in
144 each model. At the end of the *winner-take-all* learning process in the SOM, each image input vector x
145 becomes associated to its best matching model on the map m_c . The difference between x and m_c , $\|x - m_c\|$,
146 is a measure of how close the final SOM value is to the original input value and is reflected by
147 the quantization error QE. The average QE of all X_i in an image is given by

$$148 \quad QE = 1/N \sum_{i=1}^N \|X_i - m_{c_i}\| \quad (3)$$

149 where N is the number of input vectors x in the image. The final weights of the SOM are defined by
150 a three dimensional output vector space representing each R, G, and B channel. The magnitude as
151 well as the direction of change in any of these from one image to another is reliably reflected by
152 changes in the QE. The SOM training process consisted of 1 000 iterations for a two-dimensional
153 rectangular map of 4 by 4 nodes capable of creating 16 model observations from the data. The
154 spatial locations, or coordinates, of each of the 16 models or domains, placed at different locations
155 on the map, exhibit characteristics that make each one different from all the others. When a new
156 input signal is presented to the map, the models compete and the winner will be the model the
157 features of which most closely resemble those of the input signal. The input signal will thus be
158 classified or grouped in one of models. Each model or domain acts like a separate decoder for the
159 same input, i.e. independently interprets the information carried by a new input. The input is
160 represented as a mathematical vector of the same format as that of the models in the map.
161 Therefore, it is the presence or absence of an active response at a specific map location and not so
162 much the exact input-output signal transformation or magnitude of the response that provides the
163 interpretation of the input. To obtain the initial values for the map size, a trial-and-error process
164 was implemented. Map sizes larger than 4 by 4 produced observations where some models ended
165 up empty, which meant that these models did not attract any input by the end of the training. As a
166 consequence, 16 models were sufficient to represent all the fine structures in the image data.
167 Neighborhood distance and learning rate were constant at 1.2 and 0.2 respectively. These values

168 were obtained through the trial-and-error method after testing the quality of the first guess, which
 169 is directly determined by the value of the resulting quantization error; the lower this value, the
 170 better the first guess. It is worthwhile pointing out that the models were initialized by randomly
 171 picking vectors from the training image. This allows the SOM to work on the original data without
 172 any prior assumptions about any level of organization within the data. This, however, requires
 173 starting with a wider neighborhood function and a higher learning-rate factor than in procedures
 174 where initial values for model vectors are pre-selected. The approach is economical in terms of
 175 computation times, which constitutes one of its major advantages for rapid change *versus* no change
 176 detection on the basis of even larger sets of image data, prior to any further human intervention or
 177 decision making. The last image of the series from the time range here was used to train the SOM.
 178 After training, SOM-QE analysis permits determining the QE in the map output for each of the 25
 179 images of the series. The code used for implementing the SOM-QE is available in the “R-badged
 180 articles” series [8] of the journal *Software Impacts*, a collection that presents software publications
 181 that have been verified for computational reproducibility by CodeOcean, a cloud-based
 182 computational reproducibility platform that helps the community by enabling sharing of code and
 183 data as a resource for non-commercial use. Certified papers have an attached Reproducibility
 184 Badge, a permanent Reproducibility Capsule, and are listed on the CodeOcean website [8].

185 3. Results

186 The results from the SOM-QE analysis on the image time series for the two ROI are given in
 187 Table 1 as a function of the image the year was taken and the type of ROI. They show a general
 188 trend towards increase in the QE metric across images for each ROI between 1984 and 2008. The QE
 189 in the SOM output is a reliable indicator of variability in pixel color (or contrast intensity; here in
 190 this study all images were normalized for contrast intensity and did not display variability across
 191 images) as shown in our previous work.

192 **Table 1.**SOM-QE output as a function of the image year and geographic ROI.

| Year | Las Vegas City | Residential North |
|------|----------------|-------------------|
| 1984 | 0,240437503 | 0,151226618 |
| 1985 | 0,264341069 | 0,157865360 |
| 1986 | 0,271480118 | 0,155998180 |
| 1987 | 0,289065099 | 0,169213765 |
| 1988 | 0,282803632 | 0,210600120 |
| 1989 | 0,286535270 | 0,213982186 |
| 1991 | 0,303956828 | 0,219973707 |
| 1991 | 0,298541690 | 0,225406972 |
| 1992 | 0,301994751 | 0,214975264 |
| 1993 | 0,293683986 | 0,208605453 |
| 1994 | 0,304328745 | 0,221313177 |
| 1995 | 0,298240329 | 0,212630331 |
| 1996 | 0,309779114 | 0,222464495 |
| 1997 | 0,284870821 | 0,225816809 |
| 1998 | 0,291493024 | 0,223026329 |
| 1999 | 0,296067339 | 0,238731572 |
| 2000 | 0,304491317 | 0,246826836 |
| 2001 | 0,311488540 | 0,254509105 |

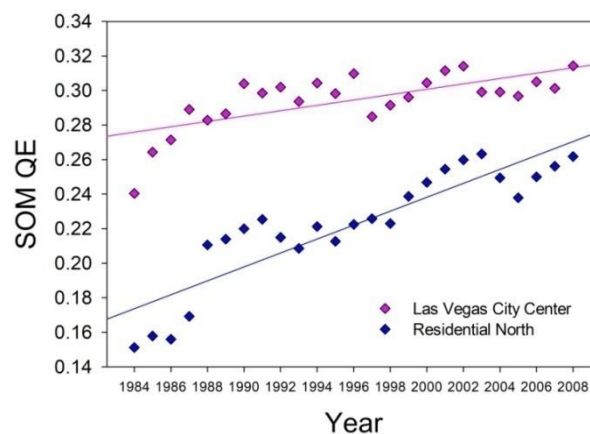
| | | |
|------|-------------|-------------|
| 2002 | 0,314104190 | 0,259835794 |
| 2003 | 0,299101833 | 0,263285485 |
| 2004 | 0,299139369 | 0,249477866 |
| 2005 | 0,296761075 | 0,237934169 |
| 2006 | 0,305053585 | 0,250044464 |
| 2007 | 0,301298833 | 0,256201407 |
| 2008 | 0,314321877 | 0,261825498 |

193

194 Here, the increase in QE captures the increasing structural variability of the landscapes, directly
 195 reflected by an increasing variability in image pixel colors, across these critical years of
 196 restructuration of Las Vegas City accompanied by the progressive building development of the
 197 Residential North. In a first analysis, these data were submitted to linear regression analysis to
 198 assess the statistical significance of the increase in QE across the years.

199 3.1. Linear regression and statistical trend analysis on the QE data

200 The linear fits to the trend in the QE to increase across the image years are shown in Figure 4.



201

202 **Figure 4.** Linear fits to the QE data as a function of the year in which a study image for a given ROI was
 203 taken.

204

205 As an estimate of the part of variance in the data that is accounted for by a linear trend, or fit, the
 206 regression coefficient r^2 is a direct reflection of the goodness of that fit. The statistical significance of
 207 the trend in the data in any given direction, upward or downward, is determined by the probability
 208 that the linear adjustment sufficiently differs from zero on the basis of Student's distribution (t). The
 209 results from the comparison QE *versus* year of image acquisition reveal a statistically significant
 210 linear trend towards increase in QE as a function of time for both ROI. The results from the linear
 211 regression analysis with the slopes and intercepts of the fits and their regression coefficients r^2 are
 212 shown in Table 2. The results from the statistical trend analyses with Student's t , Degrees of
 213 Freedom (DF) for a given comparison and the associated probability (p), limits are given in Table 3.

214

215 **Table 2.** Fit parameters from the linear regression analysis of the QE data as a function of the
 216 geographical ROI.

| Linear Fit Parameter | Las Vegas City | Residential North |
|----------------------|----------------|-------------------|
| Slope (b_1) | 1,554 | 4,0331 |
| Intercept (b_0) | -2,8077 | -7,8286 |
| r^2 | 0,4776 | 0,7995 |

217 **Table 3.** Trend statistics as a function of the geographical ROI.

| Trend Parameter | Las Vegas City | Residential North |
|-----------------|----------------|-------------------|
| t | 88,98 | 33,45 |
| DF | (1, 24) | (1, 24) |
| p | <.001 | <.001 |

218 The regression coefficients r^2 (Table 2) reveal that the linear fit to the QE data for the images of the
 219 residential North is a reasonably good one, while the linear model poorly fits the QE data for the
 220 images of Las Vegas City. This is consistent with the type of structural change that took place in
 221 each of the ROI across the study years. There was a step-by-step reorganization of the City Center,
 222 with old casinos and hotel centers disappearing one after the other to be replaced by new ones, and
 223 a much smoother, rather progressive development of buildings the in desert regions that have
 224 become part of what is now the residential North. The linear trend statistics (Table 3) reveal a
 225 statistically highly significant increase in the QE data across the image years for both ROI.

226 **3.2. Human impact data**

227 For the reference time period of this study, the Las Vegas Convention and Visitors Authority
 228 [31], and the Las Vegas Population Review [32] have provided publically archived data that show
 229 the increase of human impact across the same years as those from which the satellite images
 230 analyzed here were taken. These data are shown in Table 4 in terms of annual population estimates
 231 in thousands for Greater Las Vegas, which includes the City and the residential North, and visitors
 232 *per annum* in millions.
 233

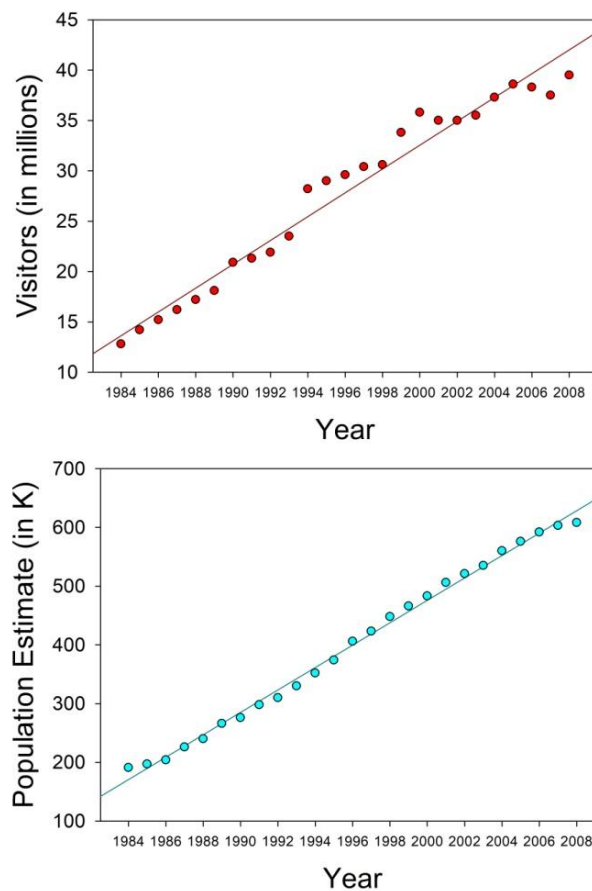
234 **Table 4.** Human impact data across the years in terms of visitor (in millions) and population
 235 (in thousands) estimates *per annum*.
 236

| Year | Visitors (in millions) | Population (in K) |
|------|------------------------|-------------------|
| 1984 | 12,8000 | 191,0000 |
| 1985 | 14,2000 | 197,0000 |
| 1986 | 15,2000 | 204,0000 |
| 1987 | 16,2000 | 226,0000 |
| 1988 | 17,2000 | 240,0000 |
| 1989 | 18,1000 | 266,0000 |
| 1991 | 20,9000 | 276,0000 |
| 1991 | 21,3000 | 298,0000 |
| 1992 | 21,9000 | 310,0000 |
| 1993 | 23,5000 | 330,0000 |
| 1994 | 28,2000 | 352,0000 |
| 1995 | 29,0000 | 374,0000 |
| 1996 | 29,6000 | 406,0000 |
| 1997 | 30,4000 | 423,0000 |
| 1998 | 30,6000 | 448,0000 |
| 1999 | 33,8000 | 466,0000 |
| 2000 | 35,8000 | 483,0000 |
| 2001 | 35,0000 | 506,0000 |

| | | |
|------|---------|----------|
| 2002 | 35,0000 | 521,0000 |
| 2003 | 35,5000 | 535,0000 |
| 2004 | 37,3000 | 560,0000 |
| 2005 | 38,6000 | 576,0000 |
| 2006 | 38,3000 | 592,0000 |
| 2007 | 37,5000 | 603,0000 |
| 2008 | 39,5000 | 608,0000 |

237

238 These data, shown graphically in Figure 5, were also submitted to linear regression and statistical
 239 trend analysis.



240

241

242

243

Figure 5. Linear fits to the human impact data as a function of the year in which the study images were taken.

244 3.3. Linear regression and statistical trend analysis on the human impact data

245

246

247

248

249

250

251

252

The results from the comparisons population estimate *versus* year of image acquisition and annual visitor estimate *versus* year reveal statistically significant linear trends towards increase as a function of time for both types of human impact data. The linear fits to the trends in these data to increase across the image years are shown in Figure 5. The results from the linear regression analysis with the slopes and intercepts of these fits and their regression coefficients r^2 are shown in Table 5. The results from the statistical trend analyses with Student's t , Degrees of Freedom (DF) for a given comparison and the associated probability (p), limits are given in Table 6.

253 **Table 5.** Fit parameters from the linear regression analysis of the human impact data in terms
 254 of visitors in millions and population (residents) in thousands *per annum*.
 255

| Linear Fit Parameter | Visitors | Population |
|----------------------|----------|------------|
| Slope (b_1) | 1,1828 | 19,0723 |
| Intercept (b_0) | -2,333 | -3766 |
| r^2 | 0,9657 | 0,9955 |

256 **Table 6.** Trend statistics as a function of the type of human impact data

| Trend Parameter | Visitors | Population |
|-----------------|----------|------------|
| t | 15,70 | 14,20 |
| DF | (1, 24) | (1, 24) |
| p | <.001 | <.001 |

257

258 The regression coefficients r^2 (Table 5) reveal that the quality of the linear fits to the human impact
 259 data across the years is excellent. The steady increase in population and visitors of Greater Las
 260 Vegas is consistent with the restructurations that took place across these years, creating an
 261 increasingly larger offer for state-of-the-art entertainment on the one hand, and a need for more
 262 residential development catering for the needs of people providing their workforce for this
 263 expanding industry. The linear trend statistics (Table 6) reveal a statistically highly significant
 264 increase in the visitors and population data across these critical years.

265 3.4. Correlation Analysis

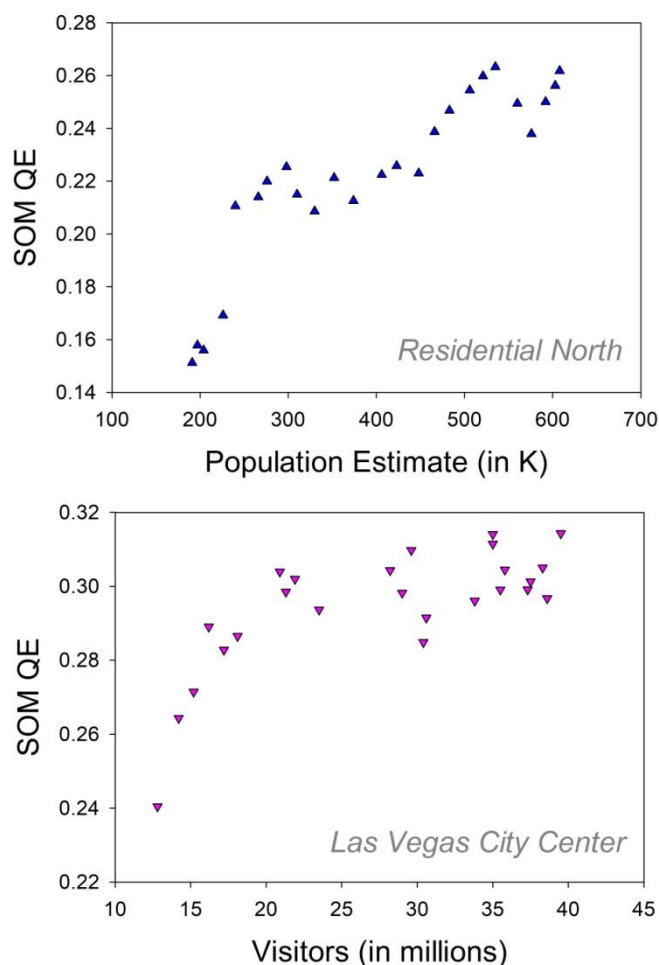
266 In the next analysis, the correlations between the QE distributions from the SOM-QE
 267 analysis and the distributions reflecting human impact data in terms of population and visitors
 268 *per annum* statistics and were computed. Correlations are useful because they may indicate a
 269 predictive relationship between variables, which then can be further exploited in practice. To
 270 that effect we computed Pearson's correlation coefficient R , which mathematically determines
 271 statistical covariance. The probability p that the covariance of two observables is statistically
 272 significant is determined by the magnitude of the Pearson coefficient, which is directly linked
 273 to the strength of correlation, while its sign is directly linked to the direction of the covariance
 274 (positive or negative) of two variables. This analysis was performed on the paired distributions
 275 for the QE from the image analysis of the residential North as a function of the population data
 276 and for the results from the image analysis of Las Vegas City as a function of the average
 277 yearly visitor estimates. The results show statistically significant positive correlations between
 278 the paired variables in both cases. The correlation statistics, with the Pearson coefficients for a
 279 given comparison and the associated DF and probability limits, are shown in Table 7.

280 **Table 7.** Pearson correlation statistics as a function of the type of comparison

| Correlation Parameter | QE North <i>vs</i> Population | QE City <i>vs</i> Visitors |
|-----------------------|-------------------------------|----------------------------|
| Pearson's R | 0,87 | 0,71 |
| DF | (1, 24) | (1, 24) |
| p | <.001 | <.001 |

281 The correlations were plotted graphically for visualization (Figure 6), showing the SOM-QE
 282 from the 25 images of the residential North as a function of the yearly population estimates

283 (Fig. 6, top) and the SOM-QE from the 25 images of Las Vegas City as a function of the annual
 284 number of visitors across the years of the reference period (Fig. 6, bottom).



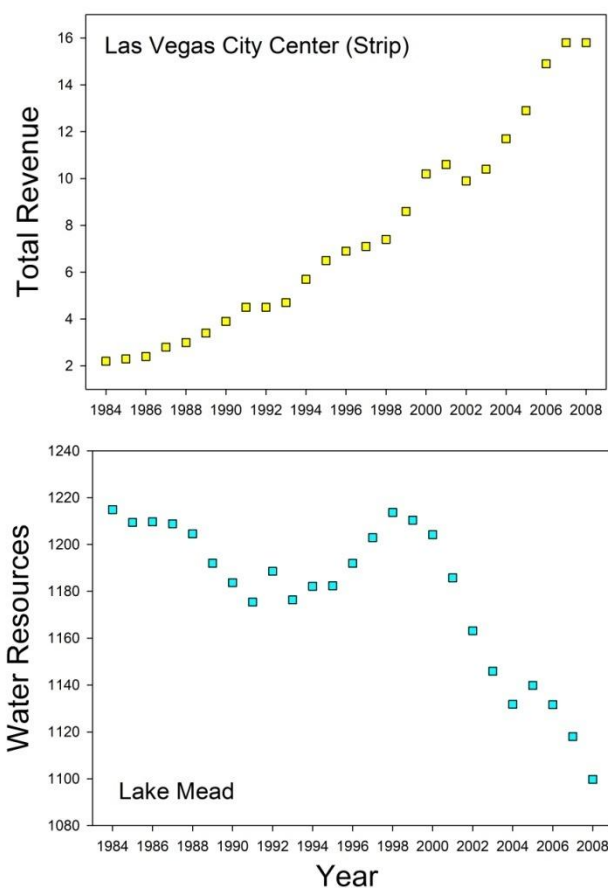
285

286 **Figure 6.** Correlation between the QE values from the image analyses and the pertinent human
 287 impact estimate for a given geographic ROI.

288 4. Discussion

289 This study is couched in the larger framework of pixel colour-based approaches to the analysis
 290 of Earth images from satellites such as Landsat to study temporal changes relating to the effects of
 291 human activities on landscape changes and/or climate change [33, 34]. Here, the SOM-QE data from
 292 analyses of satellite images of the residential North of Greater Las Vegas and the Las Vegas City
 293 Center consistently capture the anthropogenic structural changes in each ROI across the study
 294 years. The step-by-step reorganization of the City Center, with old casinos and hotel centers
 295 disappearing and replaced by more and larger new ones, and the progressive development of
 296 housing and infrastructure in desert regions that are now part of the residential North. The
 297 significant positive correlations between the QE distributions from the SOM-QE analysis and the
 298 distributions reflecting human impact data in terms of population and visitors *per annum* allow for
 299 a deeper analysis of anthropogenic movements across these critical years. The steady increase in
 300 visitors of Las Vegas City reflects the direct anthropogenic response to the increasingly larger offer
 301 of state-of-the-art entertainment in the City. This engendered an increasing need for residential
 302 development in desert regions to provide housing for an increasing population providing the
 303 necessary workforce. During these same years, the water supply to these regions dwindled away
 304 progressively, as shown in a previous study applying SOM-QE to satellite images of Lake Mead,

305 the major source of water supply to greater Las Vegas, which includes the residential North, and
 306 Las Vegas City. These observations reveal combined effects of climate change and increase in
 307 human footprint [35] on this region, bearing in mind that greater Las Vegas is one of the driest
 308 regions in the world [36]. The analyses provided here open a window for understanding the links
 309 between economic development and environmental impact in this particular region. When plotting
 310 the total revenues from gaming and leisure activities [37] of Las Vegas City Centre ('The Strip') and
 311 the water level statistics for Lake Mead provided by the Hoover Dam Control Room [38] across the
 312 years of the reference period (for illustration only here), we see a negative correlation (Pearson's R
 313 $(1,24) = -0,82$; $p < .00$) between economic development and resource availability (Figure 7).
 314



315
 316

317 **Figure 7.** Revenues from gaming and leisure activities (top) and water level statistics for Lake Mead
 318 across the years of the reference study.

319 The results from this study highlight some novel aspects of the full potential of input-driven self-
 320 organization in a parsimoniously designed neural network model (AI). SOM-QE provides a highly
 321 reliable output metric that scales, in a few minutes and with a to-the-single-pixel precision, local
 322 variability in time series of images containing millions of pixels each. Although it is self-organizing,
 323 learning in the SOM is explainable and so are its prototype design architecture and the neural
 324 workspace. The input data are not biased, and clearly defined physically. The output metric, the QE,
 325 initially used as a quality metric and for network quantization [6, 7], is proven a powerful and
 326 consistent detector of invisible local changes. When the input to a SOM is constant across time, the QE
 327 metric is invariant [6, 7]. When variability in a locally defined dimension of the input data is
 328 systematic across time, in a given direction (increase or decrease), the QE will systematically and
 329 reliably increase or decrease, as shown in the bulk of our previous work and, once again, here in this

330 study. Easily implemented, fast, and computationally economic, SOM-QE satisfies all the current
331 criteria for trustworthy and sustainable AI [39, 40], within a modest but diverse range of applications.

332 **Supplementary Materials:** The following are available online at www.mdpi.com/link: Folder S1, 50 original
333 pre-processed images from the time series of 25 images for each the two ROI.

334 **Funding:** This research received no external funding.

335 **Acknowledgments:** The authors gratefully acknowledge support from their respective host institutions.

336 **Conflicts of Interest:** The authors declare no conflict of interest.

337 References

- 338 1. Grossberg S. *Conscious Mind, Resonant Brain: How Each Brain Makes a Mind* 2021, Oxford University
339 Press.
- 340 2. Hebb, D. *The Organization of Behaviour* 1949; John Wiley & Sons: Hoboken, NJ, USA.
- 341 3. Grossberg, S. Self-organizing neural networks for stable control of autonomous behavior in a changing
342 world. In *Mathematical Approaches to Neural Networks*; Taylor, J.G., Ed.; Elsevier Science Publishers:
343 Amsterdam, The Netherlands, 1993; pp.139–197.
- 344 4. Dresp-Langley, B. Seven Properties of Self-Organization in the Human Brain. *Big Data Cogn Comput* 2020;
345 4, 10.
- 346 5. Carpenter, GA. Distributed Learning, Recognition, and Prediction by ART and ARTMAP Neural
347 Networks. *Neural Netw* 1997; 10(8), 1473-1494.
- 348 6. Kohonen T. *Self-Organizing Maps*. 2001; online: <http://link.springer.com/10.1007/978-3-642-56927-2>
- 349 7. Kohonen T. MATLAB Implementations and Applications of the Self-Organizing Map. *Unigrafia Oy*, 2014;
350 Helsinki, Finland.
- 351 8. Wandeto J, Dresp-Langley B. SOM-QE ANALYSIS - a biologically inspired technique to detect and track
352 meaningful changes within image regions. *Software Impacts* 2023; 17, 100568.
353 <https://doi.org/10.1016/j.simpa.2023.100568>
- 354 9. Liu R, Wandeto J, Nageotte F, Zanne P, de Mathelin M, Dresp-Langley, B. Spatiotemporal modeling of
355 grip forces captures proficiency in manual robot control. *Bioengineering* 2023; 10, 59.
- 356 10. Dresp-Langley B, Wandeto J. Unsupervised classification of cell-imaging data using the quantization
357 error in a self-organizing map. In: Arabnia, H.R., Ferens, K., de la Fuente, D., Kozerenko, E.B., Olivás
358 Varela, J.A., Tinetti, F.G. (eds.), *Advances in Artificial Intelligence and Applied Cognitive*
359 *Computing Transactions on Computational Science and Computational Intelligence*, pp. 201-209, Springer
360 International Publishing, Cham (2021).
- 361 11. Dresp-Langley B, Wandeto J. Human symmetry uncertainty detected by a self-organizing neural network
362 map. *Symmetry* 2021; 13, 299.
- 363 12. Dresp-Langley B, Liu R, Wandeto J. Surgical task expertise detected by a self-organizing neural network
364 map. *10.48550/arXiv.2106.08995*; 2021.
- 365 13. Dresp-Langley B, Wandeto J. Pixel precise unsupervised detection of viral particle proliferation in cellular
366 imaging data. *Informatics in Medicine Unlocked* 2020; 20, 100433.
- 367 14. Wandeto J, Dresp-Langley B. The quantization error in a self-organizing map as a contrast and colour
368 specific indicator of single-pixel change in large random patterns. *Neural Networks* 2019; 119, 273-285.
- 369 15. Dresp-Langley B, Nyongesa H, Wandeto J. Vision-inspired automatic detection of water level changes in
370 satellite images: the example of Lake Mead. *Perception* 2019; 48, ECVF Abstract Supplement.
- 371 16. Wandeto J and Dresp –Langley B. Ultrafast automatic classification of SEM image sets showing CD4 cells
372 with varying extent of HIV virion infection. *7ièmes Journées de la Fédération de Médecine Translationnelle de*
373 *Strasbourg* 2019; May 25-26, Strasbourg, France.
- 374 17. Wandeto J, Dresp-Langley B. The quantization error in a self-organizing map as a contrast and colour
375 specific indicator of single-pixel change in large random patterns. *Neural Networks (Special Issue in Honor*
376 *of the 80th Birthday of Stephen Grossberg)*, 2019; 120, 116-128.
- 377 18. Wandeto J, Nyongesa H, Dresp-Langley, B. Detection of smallest changes in complex images comparing
378 self-organizing map to expert performance. *Perception* 2017; 46, ECVF Abstract Supplement.

- 379 19. Wandeto J, Nyongesa H, Rémond Y, Dresp-Langley B. Detection of small changes in medical and
380 random-dot images comparing self-organizing map performance to human detection. *Informatics in*
381 *Medicine Unlocked* 2017; 7, 39-45.
- 382 20. Cattell JM. The influence of the intensity of the stimulus on the length of the reaction time. *Brain*. 1886;8:
383 512-515.
- 384 21. Exner S. Ueber die zu einer Gesichtswahrnehmung noetige Zeit. *Sitzungsberichte der Kaiserlichen Akademie*
385 *der Wissenschaften*, 1868; 57:601-632.
- 386 22. Green, DM, Swets, JA. *Signal detection theory and psychophysics*. 1973; Krieger Publishing, Huntington, NY.
- 387 23. Dou X, Guo H, Zhang L, Liang D, Zhu Q, Liu X, Zhou H, Lv Z, Liu Y, Gou Y, Wang Z. Dynamic
388 landscapes and the influence of human activities in the Yellow River Delta wetland region. *Sci Total*
389 *Environ* 2023; 899, 166239. doi: 10.1016/j.scitotenv.2023.166239.
- 390 24. Luke, TW. Gaming space: casinopolitan globalism from Las Vegas to Macau. In Steger, M., McNevin, A.
391 (eds.) *Global Ideologies and Urban Landscapes*, Routledge, 2013; pp. 77-87.
- 392 25. NASA/Goddard Space Flight Center Landsat images from USGS Earth Explorer. ID: 10721, Mar. 2012:
393 <http://svs.gsfc.nasa.gov/10721> last accessed 2023/09/11.
- 394 26. The VLC media player source code: <https://www.videolan.org/vlc/download-sources.html> last accessed
395 2023/09/19.
- 396 27. Dresp-Langley, B, Reeves, A. Colour for behavioural success. *i-Perception*. 2018; 9(2): 1–23.
- 397 28. Thévenaz P, Ruttimann UE, Unser MA. Pyramid Approach to Subpixel Registration Based on Intensity.
398 *IEEE Transactions on Image Processing* 1998; 7, 27–41.
- 399 29. Wieland M, Pittore M. Performance Evaluation of Machine Learning Algorithms for Urban Pattern
400 Recognition from Multi-spectral Satellite Images. *Remote Sensing* 2014; 6, 2912–2939.
- 401 30. Schneider CA, Rasband WS, Eliceiri KW. From NIH Image to ImageJ: 25 years of image analysis. *Nature*
402 *Methods* 2012; 9, 671 (2012).
- 403 31. Las Vegas Convention and Visitors Authority, Statistics: <https://www.lvcva.com/> last accessed:
404 2023/09/20.
- 405 32. Las Vegas Population Review: <https://worldpopulationreview.com/world-cities/las-vegas-population> last
406 accessed: 2023/09/20.
- 407 33. Orheim O, Lucchitta B. Investigating Climate Change by Digital Analysis of Blue Ice Extent on Satellite
408 Images of Antarctica. *Annals of Glaciology* 1990; 14, 211-215.
- 409 34. Furusawa T, Koera T, Sibirian R *et al.* Time-series analysis of satellite imagery for detecting vegetation
410 cover changes in Indonesia. *Sci Rep* 2023; 13, 8437 (2023).
- 411 35. Camacho C, Palacios S, Sáez P, Sánchez S, Potti J. Human-induced changes in landscape configuration
412 influence individual movement routines: lessons from a versatile, highly mobile species. *PLoS One* 2014;
413 9(8):e104974. doi: 10.1371/journal.pone.0104974.
- 414 36. Frumkin H, Das MB, Negev M, Rogers BC, Bertollini R, Dora C, Desai S. Protecting health in dry cities:
415 considerations for policy makers. *BMJ*. 2020; 371:m2936. doi: 10.1136/bmj.m2936.
- 416 37. University of Nevada Center for Gaming Research Annual Statistics, 2023; online at:
417 https://gaming.library.unlv.edu/reports/NV_departments_historic.pdf
- 418 38. US Department of Interior Bureau of Reclamation, Hoover Dam Control Room Statistics:
419 <https://www.usbr.gov/lc/region/g4000/hourly/mead-elv.html> last accessed: 2023/10/25.
- 420 39. Vetter D, Amann J, Bruneault F. *et al.* Lessons Learned from Assessing Trustworthy AI in Practice. *DISO*
421 2023;2, 35. <https://doi.org/10.1007/s44206-023-00063-1>
- 422 40. AI HLEG - High-Level Expert Group on Artificial Intelligence. *Assessment List for Trustworthy Artificial*
423 *Intelligence (ALTAI) for self-assessment* 2020; The European Commission.
424 https://ec.europa.eu/newsroom/dae/document.cfm?doc_id=68342
425

